ADVANCED FUNCTIONAL MATERIALS
www.afm-journal.de

# Development of Nanocarrier-Based Oral Pegfilgrastim Formulations for Mitigating Hematopoietic Acute Radiation Syndrome

*Yuefei Zhu, Daniel Naveed Tavakol, Huaxi Wang, Siyu He, Brian Ponnaiya, Zixian Zhu, Yongqiang Xiao, Naoto Yoshinaga, Xuefeng Wu, Xiaoyu Wu, Derek Ning, Ilaria Baldassarri, Diogo Teles, Sally A. Amundson, Guy Garty, David J. Brenner, Gordana Vunjak-Novakovic, and Kam W. Leong**

**The increasing risks of ionizing radiation (IR) from deep space travel and nuclear accidents necessitate the development of effective countermeasures. Acute radiation syndrome (ARS), particularly hematopoietic ARS (H-ARS), leads to life-threatening anemia and bone marrow failure, with long-term risks including cancer and cardiovascular disease. This study presents phenylboronic acid-functionalized chitosan-polyethylenimine (CPB) polymers designed for efficient oral delivery of pegfilgrastim (PF), an FDA-approved radioprotective agent. Nanoparticles are prepared through complexation of PF with tannic acid, forming a negatively charged core, followed by encapsulation with a CPB polymer shell. This supramolecular strategy enables efficient protein condensation into uniform nanoparticles. The nanosystem effectively reduces H-ARS-associated anemia in mice by promoting blood cell reconstitution, supported by in vitro results with human hematopoietic stem/progenitor cells. Additionally, the material reduces toll-like receptor activation in multiple human cell types post-radiation. This system may mitigate radiation injury risks from accidental exposure on Earth and during extended space missions.**

## 1. Introduction

Acute radiation syndrome (ARS) is characterized by severe illness following whole-body exposure to high doses of tissue-penetrating radiation over a short timeframe.[1] ARS primarily results from the rapid depletion of stem-like, metabolically-active cell types in certain tissues. Hematopoietic acute radiation syndrome (H-ARS), one of the most life-threatening manifestations of ARS, is a significant concern for both low- and high-dose-rate exposures of radiation on humans. H-ARS is marked by the rapid reduction of hematopoietic progenitor cells as a result of whole-body radiation, leading to substantial decreases in lympho-hematopoietic elements and a consequential immunosuppressive state.[2] Clinical manifestations include neutropenia, thrombocytopenia, and bone marrow (BM) hyperplasia, underscoring the need for effective medical countermeasures to mitigate radiation-induced morbidity and mortality.[3]

With increasing efforts from NASA to send astronauts on deep space missions to the Moon and Mars, mitigating hematopoietic risks is critical for preventing both acute injury and chronic disease in humans.[4] H-ARS is one of the major concerns for space travel, as previous studies have indicated risks associated with high-linear energy transfer radiation and the development of anemia and cancer.[5] Further, the development of rapid countermeasures is essential to treat accidental exposures to radiation on Earth, as well as protect civilians from the increasing risks of biological and nuclear warfare.[6]

Y. Zhu, D. N. Tavakol, H. Wang, S. He, Z. Zhu, Y. Xiao, N. Yoshinaga, X. Wu, X. Wu, D. Ning, I. Baldassarri, D. Teles, G. Vunjak-Novakovic, K. W. Leong
Department of Biomedical Engineering
Columbia University
New York, NY 10025, USA
E-mail: kam.leong@columbia.edu

The ORCID identification number(s) for the author(s) of this article can be found under https://doi.org/10.1002/adfm.202421462

**DOI: 10.1002/adfm.202421462**

B. Ponnaiya, S. A. Amundson, G. Garty, D. J. Brenner
Center for Radiological Research
Columbia University
New York, NY 10032, USA

G. Vunjak-Novakovic
Department of Medicine
and College of Dental Medicine
Columbia University
New York, NY 10032, USA

K. W. Leong
Department of Systems Biology
Columbia University
New York, NY 10032, USA

 

Pegfilgrastim (PF), a pegylated form of granulocyte colony-stimulating factor, received FDA approval for mitigating the risk of radiation syndrome, marking a significant advancement in treatment protocols for acute radiation syndrome since March 2015.[7] This therapeutic agent is effective in promoting both self-renewal and differentiation of hematopoietic stem/progenitor cells (HSPCs), a process known as hematopoiesis, thus facilitating the recuperation from radiation-induced damage to the hematopoietic system.[8] Notably, PF demonstrates an extended in vivo half-life of approximately 42 h, which significantly surpasses the 3.5 h half-life of its non-pegylated counterpart, filgrastim.[9] Despite its efficacy, PF's application is restricted to subcutaneous administration. While effective, the parenteral administration requires the involvement of healthcare provider and decreases patient compliance.[10] In contrast, oral administration offers considerable advantages in terms of cost and ease of administration, potentially improving patient compliance. In addition, administration of oral drugs provides an advantage for potential deep-space missions, reducing the burden of medical administration by astronauts or single-person voyages.

Here, we describe a novel, oral formulation of PF, aiming for a noninvasive and effective radioprotection from H-ARS.[11] Despite extensive research into oral protein delivery, with chitosan (CS) and its derivatives as one of the attractive carriers, efficiency has remained suboptimal. Optimal oral protein carriers should safeguard encapsulated proteins across a diverse pH spectrum, traverse the gut epithelium effectively, and facilitate efficient intracellular delivery via endosomal escape and payload release.[12] This study proposes the design of phenylboronic acid (PBA)-functionalized chitosan polymers modified with low molecular weight branched polyethylenimine (CS-PEI, denoted as CP). The reduced toxicity of low molecular weight PEI augments chitosan's permeation efficiency across gut epithelium without increasing cytotoxicity. The dual-responsive nature of PBA enhances polyplex stabilization in acidic environments, improves mucosal transport, and boosts endosomal escape and cytosolic release in targeted cells.

The nanoparticles feature a shell of phenylboronic acid (PBA)-functionalized CS-PEI (CPB) and an inner core composed of PF and tannic acid (TA). Tannic acid, a naturally occurring antioxidant polyphenol derived from oak tree galls, exhibits a strong affinity for proteins through hydrogen bond interactions.[13] This property is beneficial for protein delivery.[14] Unlike nucleic acid drugs, which can strongly interact with cationic materials through electrostatic attractions, facilitating their condensation into nanoparticles and cellular uptake.[15] Proteins, in contrast, typically display less pronounced charges and do not interact as uniformly with cationic materials.

To address this, our nanoparticles were synthesized through initial precomplexation of PF with TA, forming a negatively charged core, which was then encapsulated by a low-molecular-weight cationic polymer to create the shell. This supramolecular approach condenses proteins into uniform nanoparticles, achieving 86.7% encapsulation efficiency, 13% loading capacity, and minimal toxicity in both in vitro and in vivo assays. Based on this formulation, we developed and evaluated a library of CPBs with varying grafting ratios of BPEI and PBA decoration to optimize the oral delivery efficiency of PF.

To validate the NPs, we tested their cytocompatibility using human cord blood (CB)-derived HSPCs and intestinal cell lines, as well as in vitro efficacy by characterizing the neutrophil differentiation capacity of human CB-HSPCs exposed to the NPs and control derivatives. In addition, we confirmed the ROS scavenging capabilities of the CPB formulation using a number of human cell types, including cardiomyocytes, endothelial cells, and fibroblasts. Finally, we tested the oral PF NP formulations for in vivo toxicity and efficacy in murine models of hematopoietic injury, using a lethal dose of radiation and PF as the gold standard for comparison. Through this, we identified an optimized nanoformulation that effectively delivers PF orally for mitigating H-ARS.

## 2. Results

### 2.1. Construction and Profiling of Polymer and Nanoparticle Library

Constructs of CS-PEI (CP) were synthesized incorporating specific grafting ratios of branched polyethyleneimine (BPEI) at 39% and 72%. These graft polymers were further modified by conjugating phenylboronic acid in varying proportions through amide coupling, aimed at fine-tuning the intracellular unpacking of the NPs. This strategy was also designed to protect the encapsulated PF from the acidic conditions prevalent in the gastrointestinal environment, as illustrated in **Figure 1A**.

The polymer synthesis steps are illustrated in Figure S2 (Supporting Information). The composition of the polymers was confirmed by $^{1}$H NMR spectroscopy, with a representative NMR image provided in Figure S3 (Supporting Information), and corroborated by FTIR spectroscopy results, shown in Figure S4 (Supporting Information). This process resulted in the generation of a library of 14 PBA-functionalized chitosan-polyethyleneimine polymers, designated as $CP_{X\%}B_{Y\%}$, where X and Y denote the mass percentages of BPEI grafting and PBA functionalization, respectively (Table S1, Supporting Information).

In a preparatory step before complexation with CP, TA was pre-incubated with PF to exploit its polyphenolic structure for establishing a strong, non-covalent bond with the protein via hydrogen bonding and hydrophobic interactions. This affinity was confirmed through molecular docking and dynamic simulation analyses. Furthermore, the versatility of CPB as a general protein delivery system was assessed using bovine serum albumin (BSA) and insulin as representative proteins, with their simulated crystal structures illustrated in Figure S5 (Supporting Information). This evaluation highlighted CPB's capability for rapid self-assembly into CPB@protein nanoparticles within an aqueous milieu, notably without the necessity for organic solvents, as depicted in Figure 1B and Figure S1 (Supporting Information).

The $CP_{72\%}B_{24\%}$@PF group displayed an average hydrodynamic size of 112.57±0.40 nm (Figures 1E and 2A) and spherical morphology, as confirmed by transmission electron microscopy (TEM) images (Figure 1C). A zeta potential of 5.66 ± 0.09 mV indicated a lowered charge density compared with CP due to the PBA functionalization. The cytotoxicity profile, assessed via the CCK-8 assay on HSPCs and supplemented by live-dead cell assays, showed a reduction in cytotoxicity following PBA modification (Figures S9 and S10, Supporting Information). The

 

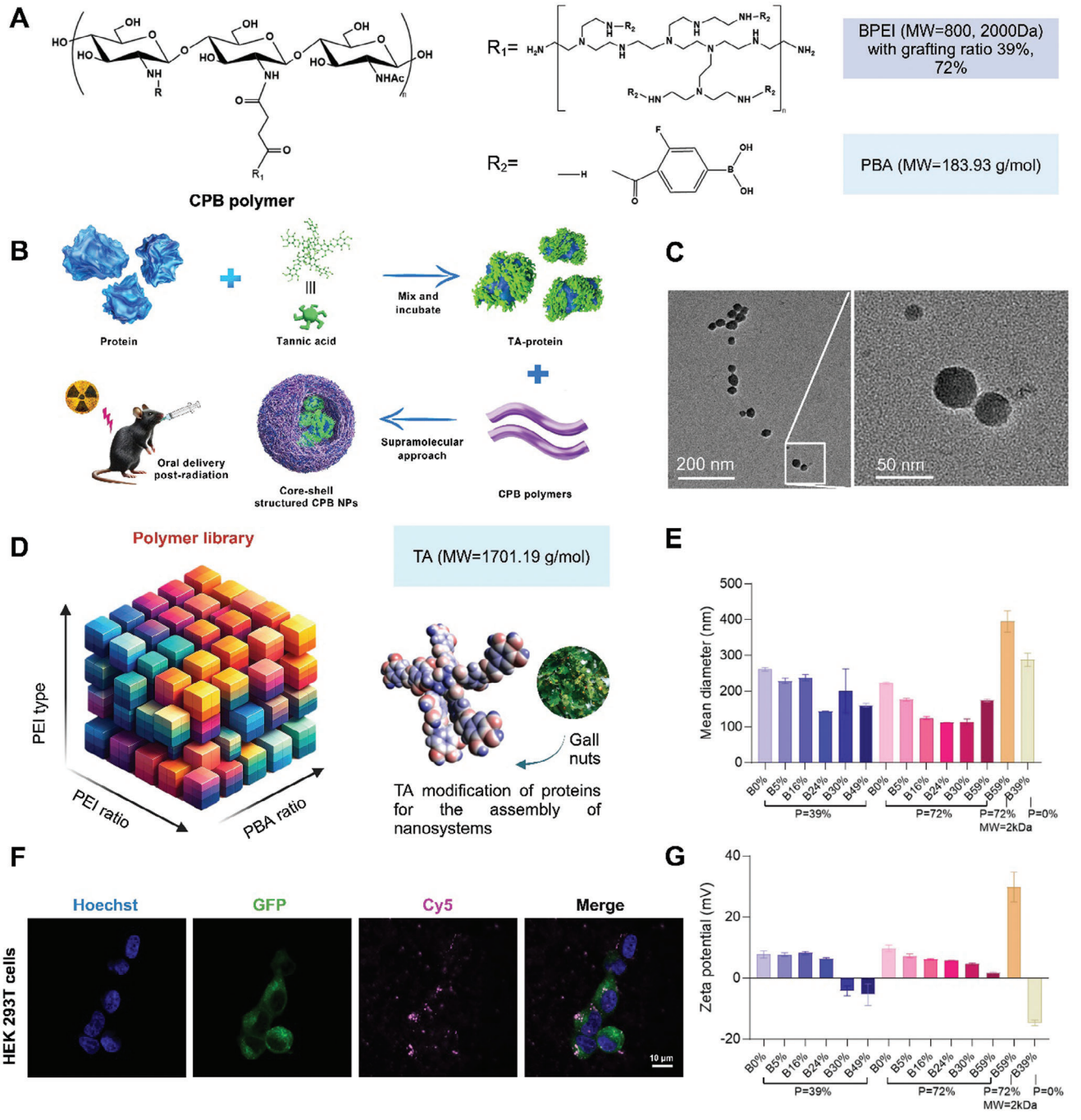


**Figure 1.** Construction and profiling of CPB polymer and CPB@PF library. A) Synthetic scheme of CPB. B) Schematic diagram of the nanoparticle assembly process for oral protein delivery. C) Representative transmission electron microscopy (TEM) images of CPB@PF NPs, which were visualized using a negative staining technique with Uranyless stain. Scale bars, 200 nm and 50 nm. D) Schematic illustration of the polymer library established for PF delivery. The polymer was varied by modulating the PEI and PBA grafting ratio, with the addition of TA as an auxiliary for efficient assembly with PF. The tannic acid figure is adapted from "Tannic acid ESP" by Mplanine, available on Wikimedia Commons, used under CC BY-SA 4.0. The gall nuts figure is adapted from a photograph by Olga Ilina/Shutterstock (Confirmation Number CS-0A157-35B9), used under license. E) Hydrodynamic particle size of the polymer library, including CPB@PF NPs, CP@PF NPs, and CB@PF NPs. Data are presented as the mean ± SD from $n = 3$ replications. F) CLSM images of the HEK 293T cells at 24 h after being treated with CPB@PF NPs. The Cy5 labeled CPB starts to escape from the late endosome compartment. Scale bar, 10 μm. G) Zeta potential of the polymer library, including CPB@PF NPs, CP@PF NPs, and CB@PF NPs. Data are presented as the mean ± SD from $n = 3$ replicates.

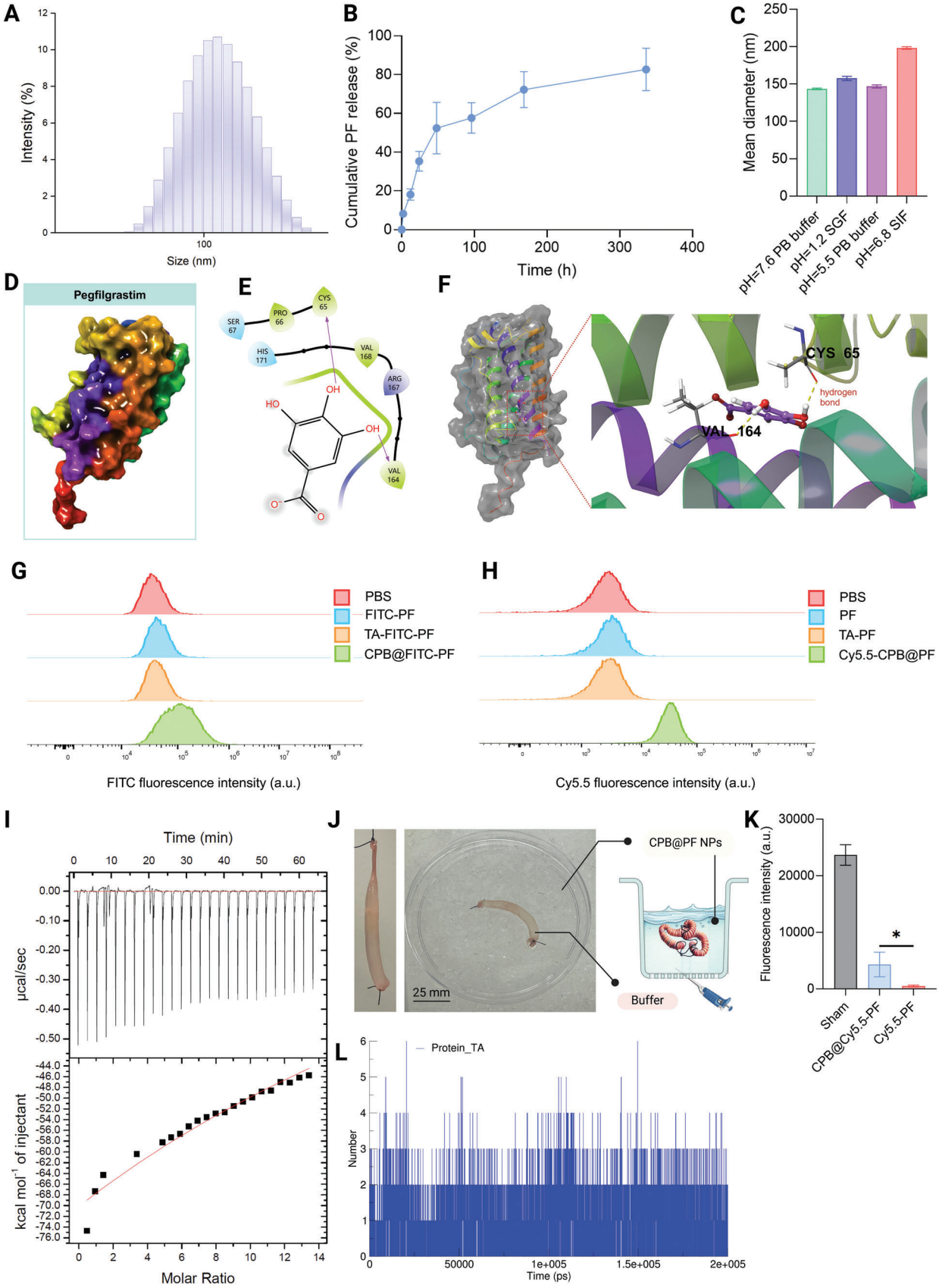

CPB@PF library's cytotoxicity evaluation revealed a higher $IC_{50}$ for $CP_{72\%}B_{24\%}$@PF (458.9 μg $mL^{-1}$), underscoring the benign nature of the low-concentration TA and the lower overall charge density of the NPs (Figure S10, Supporting Information).

The acidic endosomal conditions lead to the protonation of the amine groups within CP, instigating a "proton sponge" effect that induces endosomal rupture,[16] facilitating the release of the encapsulated cargo into the cytosol. The incorporation of PBA enhances the internalization of nanoparticles through reversible binding to sialic acid residues on cell surface glycoproteins, promoting more robust interactions between nanoparticles and the cell surface.[17] This characteristic is beneficial for the oral delivery of pharmaceutical formulations, as 4-carboxy-3-fluorophenylboronic acid, with its acid dissociation constant (pKa) of 7.2, engages with intracellular ATP in the cytosolic pH.[18] Concurrently, it forms a hydrophobic structure (Figure S2B, Supporting Information) under the acidic pH conditions of the late endosome, instigating the destabilization of the endosomal membrane—an essential step for intracellular delivery.[19] We confirmed proficient endosomal escape capacity of the $CP_{72\%}B_{24\%}$@PF nanoparticles in HEK293T and THP-1 cell lines (Figure 1F and Figure S23, Supporting Information).

### 2.2. In Vitro Characterization of CPB@PF NPs

For subsequent analyses, the term CPB refers to $CP_{72\%}B_{24\%}$, which was selected for in vivo evaluation. We assessed the colloidal stability of CPB@PF nanoparticles in simulated gastric fluid (SGF) and intestinal fluid (SIF). The nanoparticles maintained a consistently small size in acidic conditions over a 2 h period, whereas a modest increase in size was observed in SIF following a 2 h incubation (Figure 2C). This phenomenon can be attributed to the enhanced hydrophobicity conferred by the PBA components at lower pH levels, which likely promotes closer association of the polymer chains, resulting in a denser nanoparticle structure. Conversely, at elevated pH levels, an increase in hydrophilicity facilitates the expansion of the polymer network and coincides with the commencement of protein release, thereby explaining the observed size variation. The cationic properties of CPB promote a compact core-shell formation with the anionic TA-protein complex, inhibiting premature gastric degradation and release. Enhanced by the hydrophobic PBA moiety, these nanoparticles exhibit stability across the pH gradient of the gastrointestinal tract, effectively protecting the encapsulated protein from a pH of 1.5 in the stomach and of 7.5 in the intestine. The stabilization effect is further supported by the charge density provided by grafted BPEI and the hydrophobic interactions between PBA moieties under acidic conditions (Figure 2C). CPB@PF nanoparticles appeared to undergo gradual dissociation during permeation, with CPB interacting with the epithelial layer to facilitate protein cargo penetration and subsequent release into the bloodstream. In vitro drug release studies demonstrated sustained release of the encapsulated PF over 300 h (Figure 2B).

To elucidate the mechanism of nanoparticle assembly and interaction with proteins, we used molecular docking techniques to simulate the interaction between the PF protein and monomers derived from prevalent materials employed in protein complexation. This screening encompassed a diverse array of materials, such as hyaluronic acid, alginate, poly(lactic-co-glycolic acid) (PLGA), heparin, polycaprolactone (PCL), poly(vinyl alcohol) (PVA), and tannic acid for forming the NP core. Notably, TA distinguished itself by achieving the highest docking score, as detailed in Figure S7 and Table S2 (Supporting Information). Within our devised system, TA forms a precursor complex with PF, resulting in a stable, negatively charged core. This core is subsequently enveloped by the cationic CPB polymer, culminating in the formation of the nanoparticle's shell. Employing an XP flexible docking strategy, molecular docking facilitated high-resolution analysis, pinpointing precise interactions between tannic acid monomers and PF, with a docking score suggestive of robust ligand-protein binding dynamics (Table S2, Supporting Information). This interaction is characterized by hydrophobic forces and hydrogen bonding between the monomer constituents (specifically gallic acid) and the amino acid residues of the PF protein, thus reinforcing the stability of this interaction (Figure 2D–F and Figure S6, Supporting Information). Extending this methodology to include alternative proteins, such as BSA and insulin, yielded favorable docking scores, particularly notable with insulin, suggesting the formation of stable complexes between tannic acid and these proteins (Figure S6 and Table S2, Supporting Information). This evidence supports the versatility of the assembly method in producing protein-encapsulated nanoparticles. Subsequent synthesis of CPB@BSA and CPB@insulin nanoparticles further validated this approach, demonstrating a remarkably uniform nanoparticle size

**Figure 2.** In vitro characterization of CPB@PF NPs for oral delivery. CPB refers to $CP_{72\%}B_{24\%}$ selected for both in vivo and in vitro studies. A) Hydrodynamic particle size of the CPB@PF nanoparticles. B) Cumulative PF release study in the PBS buffer. C) CPB@PF stability test in different buffers after 2 h. D) Simulated PF crystal structure using Alphafold2. E) 2D and F) 3D molecular docking analysis between PF and the tannic acid monomer. The monomer (identified as gallic acid) engages with the active pocket surface of PF, with PF protein residues, including VAL164, VAL168, and CYS65, exerting a hydrophobic influence on gallic acid. Additionally, the ligand establishes hydrogen bonds with VAL164 and CYS65 residues, further corroborating the stability of the interaction. G) Flow cytometric analysis was conducted on Caco-2 cells after treatment with various formulations, assessed based on FITC fluorescence intensity. The treatments included phosphate-buffered saline (PBS, red), FITC-labeled protein (FITC-PF, blue), TA-complexed FITC-labeled protein (TA-FITC-PF, orange), and nanoparticles loaded with FITC-labeled protein (CPB@FITC-PF, green). H) Parallel analysis based on Cy5.5 fluorescence intensity. Treatments include PBS (red), protein formulation (PF; blue), TA-complexed protein (TA-PF; orange), and Cy5.5-labeled polymer which formed NP with protein (Cy5.5-CPB@PF; green). I) Isothermal Titration Calorimetry (ITC) data of the interaction between TA-PF complex NPs and CPB polymer: power–time curve (top), showing the heat flow during consecutive injections of the CPB solution into the TA-PF solution. Integrated heat data plotted against the molar ratio of the polymer to the TA-PF complex (bottom), indicating an exothermic binding reaction. The negative peaks in the power–time curve correspond to the exothermic heat release upon each injection, and the red line in the integrated heat plot represents the best fit to a binding model, suggesting a spontaneous and energetically favorable interaction. J) Schematic illustration of the protein-penetration across everted intestine assay. K) The Cy5.5 fluorescence inside the everted gut sac at the 6 h time point. Data are analyzed by one-way ANOVA in GraphPad Prism. *p* value style: $*p < 0.05$. Data are presented as mean ± SD ($n = 3$). L) Molecular dynamics simulation of extracted hydrogen bonds to probe the interaction between PF and TA.

distribution within the 100–200 nm range (Figures S18 and S19, Supporting Information). This indicated the efficacy of an accessible assembly technique in generating protein-loaded nanoparticles with potential for broad biomedical applications.

Molecular dynamics (MD) simulations have provided insight into the molecular basis of the affinity between tannic acid and the PF protein, revealing a complex interplay of hydrogen bonding and hydrophobic interactions that underpin a robust binding mechanism (Figure 2I). To further investigate this interaction process, simulations between TA molecule and the PF protein (Figure S8, Supporting Information) were conducted to dissect the nuances of the interaction process. The simulations revealed key insights into the energetic and structural dynamics of these interactions, including energy trajectories, root-mean-square deviation (RMSD) profiles showing initial fluctuations stabilizing over time, and radius of gyration (*Rg*) trends that highlighted transient expansions and subsequent equilibration of the complex. Furthermore, a detailed 3D representation accentuated the interactive conformations between the PF protein and tannic acid, with an elaborate interaction schematic pinpointing specific amino acids within the active site of the PF engaged in binding (Figure S8E, Supporting Information). Isothermal titration calorimetry (ITC) corroborated these interactions as exothermic, indicating that the binding of CPB polymer to the TA-PF complex is energetically favorable and primarily driven by enthalpy, consistent with strong hydrogen bonds and Van der Waals forces.

The cellular uptake of the nanoparticles was further investigated using Caco-2 intestinal epithelial cells. Flow cytometry revealed a 31.7% increase in the uptake of FITC-labeled PF following nanoparticle exposure compared to the control group (Figure 2G and Figure S12, Supporting Information). This increase may be attributed to the cationic nature of the nanoparticles, which likely facilitates greater cellular uptake.[20] A similar trend was observed using Cy5.5-labeled CPB polymer, where the elevated Cy5.5 signal indicated enhanced cellular uptake (Figure 2H). To determine the potential for transmucosal delivery of PF, we assessed the paracellular intestinal permeability using the everted gut sac model, an in vitro intestinal absorption studies.[21] Our findings demonstrated that the transmembrane movement of Cy5.5-labeled PF, when assembled with CPB into nanoparticles, surpassed that of the naked protein, suggesting that the nanosystem significantly improves intestinal permeability (Figure 2J,K). Notably, the in vitro tight junction opening study corroborates these findings. We first examined the effect of CPB@PF NPs on the integrity of tight junctions by measuring the transepithelial electrical resistance (TEER), a standard technique to assess the function of the epithelial barrier.[22] The addition of CPB@PF NPs reduced the TEER to 71.8% of its initial value (Figure S14, Supporting Information), indicating partial disruption of tight junctions. In contrast, the pure protein alone did not significantly alter the TEER. Notably, TEER recovered after NP removal, demonstrating that the nanoparticles transiently open tight junctions without causing irreversible damage to the epithelial barrier. Further confirmation came from confocal fluorescence imaging, which revealed ZO-1 protein translocation and disruption of the intact green network structure (ZO-1 staining) in Caco-2 monolayers treated with CPB@PF NPs (Figure S15, Supporting Information). Skeleton-based image analysis revealed that tight junction openings occurred within 2 hours of NP treatment. Correspondingly, ZO-1—a key tight junction protein—displayed marked disorganization, consistent with reports that chitosan-based polymers can loosen tight junctions and enhance paracellular permeability.[23]

### 2.3. CPB Polymers as Dual Scavengers for Mitigating Radiation-Induced Inflammation In Vitro

Here, we focus on the potential of CPB polymers to ameliorate excessive cytokine storms triggered by TLR overactivation and consequent oxidative stress. Previous studies have shown that cfDNA levels exhibit significant elevation in primate models, mirroring those in BM transplant patients subjected to supralethal radiation doses, where cfDNA concentrations increase exponentially with radiation dose.[24] Initially, we found that both the CPB polymer and nanoparticle platform exhibit unique affinities for binding cfDNA, which is useful for mitigating inflammation (**Figure 3A**). To further explore their therapeutic potential, we assessed the impact of CPB@PF polymers on TLR activation, confirming their immunomodulatory effects. Utilizing HEK-TLR reporter cells for TLR3, TLR4, TLR8, and TLR9, exposed to specific TLR agonists (Poly(I:C) dsRNA, Lipopolysaccharide (LPS), R848, and CpG DNA), respectively, we observed that the cationic nature of CPB polymers significantly inhibits the activation of these TLRs (Figure S21, Supporting Information). This inhibition suggests a promising anti-inflammatory mechanism through cfDNA scavenging. By using FITC-labeled CpG and Cy5-labeled CPB, there was colocalization of polymer within the endolysosomes of RAW264.7 cells, indicating that CPB internalization through endocytosis could interfere CpG recognition by macrophages (Figure S20, Supporting Information).

Our study on the ROS scavenging efficiency of CPB polymers, TA-BSA, and CPB@BSA NPs reveals distinct effectiveness across varying concentrations. TA-BSA demonstrated superior performance in superoxide ($\bullet O_2^-$) scavenging at higher concentrations (75 and 37.5 μg $mL^{-1}$), with a noted decrease in effectiveness at lower concentrations (Figure S16A, Supporting Information). In the context of 1,1-diphenyl-2-picrylhydrazyl (DPPH) radical scavenging, $CP_{72\%}B_{24\%}$ showcased the highest activity at 75 μg $mL^{-1}$, though its efficiency markedly decreased at reduced concentrations. CPB@BSA NPs exhibited a more consistent decrease in efficiency across concentrations (Figure S16B, Supporting Information). For hydroxyl (•OH) radical scavenging, all tested agents consistently demonstrated high activity, underscoring their potent capacity to mitigate •OH radicals (Figure S16C, Supporting Information). A radar chart summarizing these findings highlights dominance in $\bullet O_2^-$ scavenging of TA-BSA, and the balanced ROS scavenging profile of CPB@BSA NPs across all tests (Figure S16D, Supporting Information).

Subsequent experiments explored the intracellular ROS scavenging capabilities of CPB within HCT116 and Caco-2 cells stimulated by Rosup, a chemical mixture engineered to promote ROS generation. This revealed a dose-dependent augmentation in the scavenging activity, as illustrated in Figure 3B and Figure S13 (Supporting Information). Specifically, in HCT116 cells, incremental increases in CPB concentration from 100 to 1000 μg $mL^{-1}$ across treatment periods of 0.5 and 1 h were associated with a notable decrease in ROS levels. The most significant reduction in

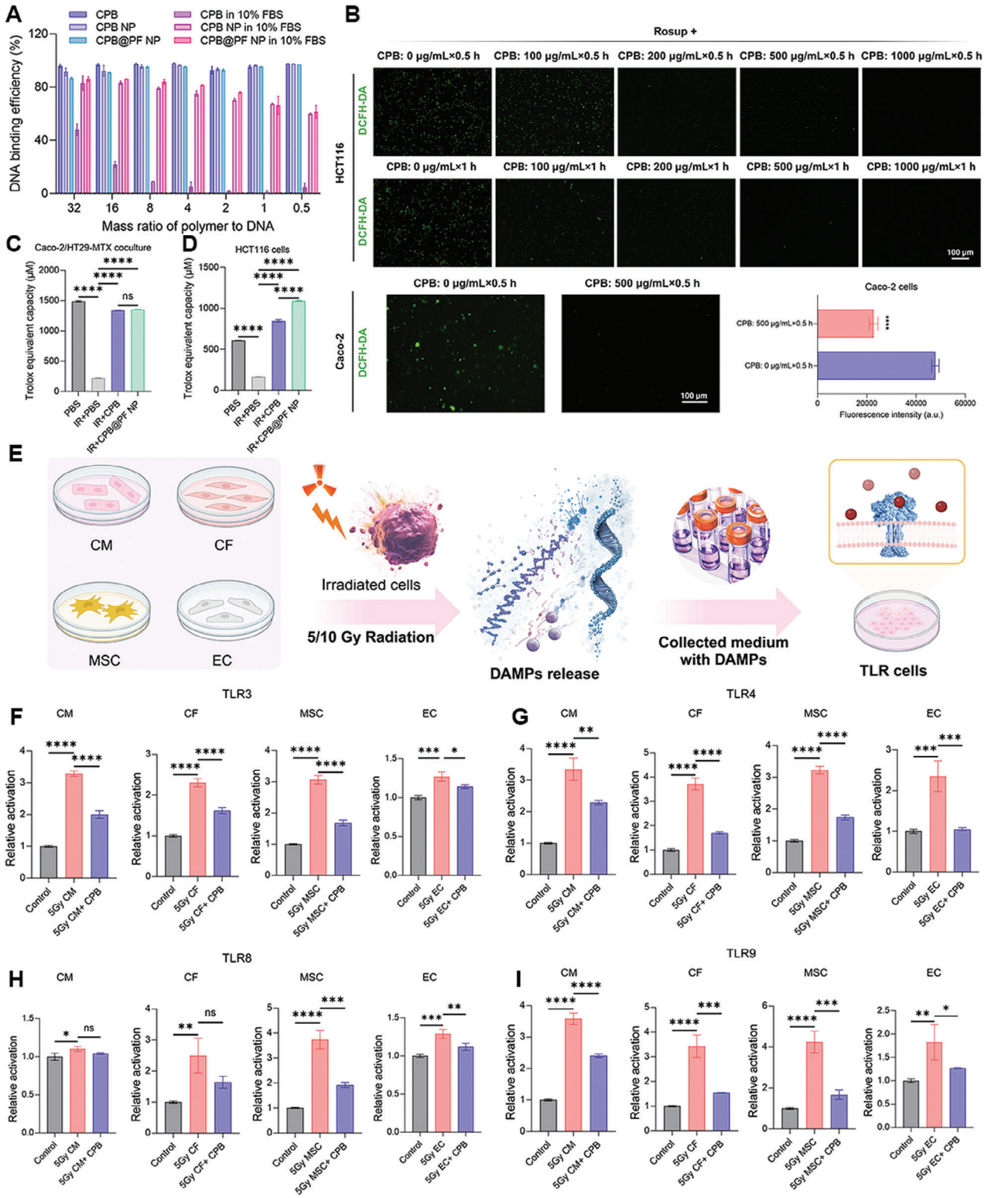


**Figure 3.** CPB polymers as innovative dual scavengers for in vitro radiation-induced inflammation mitigation. CPB refers to $CP_{72\%}B_{24\%}$ selected for both in vivo and in vitro studies. A) DNA-binding efficiency of CPB polymer, CPB NP (formed by just complexing with TA), and CPB@PF NP in PBS and 10% FBS at 37 °C. B) Fluorescence images of intracellular ROS (green) in Rosup-stimulated HCT116 and Caco-2 cells incubated with CPB polymers at various concentrations for 0.5 or 1 h. Scale bar, 100 μm. The figure in the lower right corner quantifies the fluorescence intensity of Caco-2 cells accordingly. C) Trolox equivalent antioxidant capacity of CPB and CPB@PF NPs after treating the irradiated Caco-2/HT29-MTX coculture cells and D) Trolox equivalent antioxidant capacity of CPB and CPB@PF NPs after treating the irradiated HCT116 cells E) Schematic representation of the experimental procedure.

ROS was observed at the highest concentration of 1000 μg $mL^{-1}$ after 0.5 h. In Caco-2 cells, we observed the scavenging effect at a reduced concentration of 500 μg $mL^{-1}$ after 0.5 h. These findings were further substantiated by fluorescence intensity measurements, which highlighted a marked decrease in ROS levels concomitant with escalating CPB concentrations. The total antioxidant capacity of the CPB@PF system was evaluated using a Caco-2/HT29-MTX coculture model and HCT116 cells. The investigations revealed that both the CPB polymer and its nanoparticle-based formulation, CPB@PF, exhibited an enhancement in antioxidant capacity, nearly sevenfold greater than that measured by Trolox equivalent antioxidant capacity (TEAC), as depicted in Figure 3C,D. A parallel assessment using LPS on RAW264.7 cells corroborated these results, reinforcing the notion that CPB exhibits a significant modulatory effect on inflammatory processes (Figures S24 and S25, Supporting Information).

We expanded our investigation into the scavenging capabilities of our polymers by exposing multiple human cell types to either 5 Gy or 10 Gy of radiation, including cardiomyocytes (CMs), cardiac fibroblasts (CFs), mesenchymal stem/stromal cells (MSCs), and endothelial cells (ECs) (Figure 3E). Using conditioned media from these cultures, we assessed their impact on the activation of TLR3, TLR4, TLR8, and TLR9, with and without CPB treatment. Notably, the CPB polymer formulation exhibited superior efficacy in inhibiting the activation of these four TLR pathways (Figure 3F–I and Figure S22, Supporting Information).

To confirm these findings in mice, primary splenocytes were isolated from C57BL/6 mice and subjected to radiation exposure at a dosage of 5 Gy. This model served to evaluate the therapeutic potential of CPB and CPB@PF nanoparticles in mitigating radiation-induced oxidative stress (Figure S17A, Supporting Information). Post-treatment observations highlighted an escalation in oxidative stress markers, followed by a notable reduction in green fluorescence intensity, indicative of the capacity of CPB formulations to effectively counteract oxidative stress (Figure S17A,B, Supporting Information). This evidence confirms the significant antioxidative properties of the CPB@PF system, proposing its utility in managing oxidative stress-related challenges.

### 2.4. In Vitro Neutrophil Production Induced by CPB@PF Nanoparticle Protein Release

To confirm the ability of the CPB@PF nanoparticles to release PF for recovery of hematopoietic cells after radiation injury, we tested the efficacy of the nanoparticles in comparison to protein-only and untreated controls on CB-HSPCs. After expansion, HSPCs were irradiated with 5 Gy of photons and treated with either PF protein alone, CPB@PF nanoparticles (at 25 and 50 ng $mL^{-1}$ concentrations), unconjugated PF protein with TA, and CPB protein only, in comparison to healthy HSPCs and irradiated, non-drug treated HSPCs (**Figure 4A**). After 7 and 14 d alike, $CD45^+$ hematopoietic cells were able to proliferate within both the PF- and CPB@PF groups at similar levels, significantly increasing cell proliferation recovery as compared to the irradiated (no drug) controls (Figure 4B). This effect was most pronounced by day 14, where cell recovery stabilized post-injury. As PF is known to cause an increase in granulocytes acutely, and in turn increasing the progenitor fraction of hematopoietic cells when administered to humans, we attempted to characterize the production of early- and mature- neutrophils by flow cytometry. By day 7, irradiated $CD45^+$ cells treated with CPB@PF nanoparticles were able to reach similar percentages to pure PF-treated cells, which were both significantly higher than untreated controls (Figure 4C,D). We confirmed the presence of early granulocytes and maturing neutrophils with Wright-Giemsa staining on cells isolated from these cultures (Figure 4E).

### 2.5. In Vivo Pharmacokinetics and Efficacy of the CPB@PF System

To investigate the protective effect against H-ARS of our formulations, the C57BL/6 mice were exposed to a fatal dose (7.25 Gy) of whole-body irradiation (**Figure 5A**). Various formulations were administered to the animals via oral gavage (i.g.: intragastric) or subcutaneous injection (s.c.) around 2 d post-irradiation. Mice were preconditioned with oral gavage of PBS to acclimate them to the procedure for 4 d. Post-irradiation, treatments were administered every 2 d for one week. CPB@PF NPs were administered with a PF dosage of 8.33 mg $kg^{-1}$, while for the PF (s.c.) group, we injected 15 μg for each mouse. CPB@BSA served as a control to compare the efficacy difference between the delivery of PF. We then examined the absorption sites of our oral PF at different post-gavage time points in an ex vivo fluorescent imaging study (PF labeled with Cy5.5) (Figure 5B). Control groups (PBS and free Cy5.5-labeled PF) were included for direct comparison. Minimal fluorescence was observed in the PBS group, likely due to slight background signals from ingested feed. In contrast, orally administered free Cy5.5-PF exhibited moderate fluorescence that transitioned from the stomach at 2 h to the intestines between 4 and 6 h but diminished by 8 h. In comparison, CPB@Cy5.5-PF NPs exhibited a stronger and more prolonged fluorescent signal. At 2 h post-gavage, fluorescence was primarily localized in the stomach. By 4 and 6 h, the signal had progressed into the intestines, confirming PF transit through the gastrointestinal tract. Notably, at 8 h post-gavage, substantial fluorescence remained in the lower intestines, indicating prolonged retention of the protein. This is likely due to the gradual release and absorption of the protein from the nanoparticles. This retention could be indicative of the potential of NPs to deliver PF orally within the gastrointestinal environment. For serum PF concentration monitoring, the mice were administered orally at around 8.33 mg $kg^{-1}$ of CPB@PF NPs, followed by measurement of serum PF concentration using human PF ELISA assay (Figure 5C). Mice receiving 8.33 mg $kg^{-1}$ free PF solution were used as controls. For serum PF concentration monitoring, CPB@PF NPs were administered

Cardiomyocytes (CM), cardiac fibroblasts (CF), mesenchymal stem cells (MSC), and endothelial cells (EC) were exposed to 5 or 10 Gy of irradiation. Irradiation-induced cellular damage led to the release of DAMPs, which were collected from the culture medium and used in TLR activation assays. F–I) Radiation-induced activation of TLR3, TLR4, TLR8, and TLR9 in CM, CF, MSC, and EC assessed in HEK-TLR reporter cells. The treated groups included cells exposed to 5 Gy radiation with or without CPB treatment ($n = 3$). Data represent relative activation levels of each TLR across the different cell types.

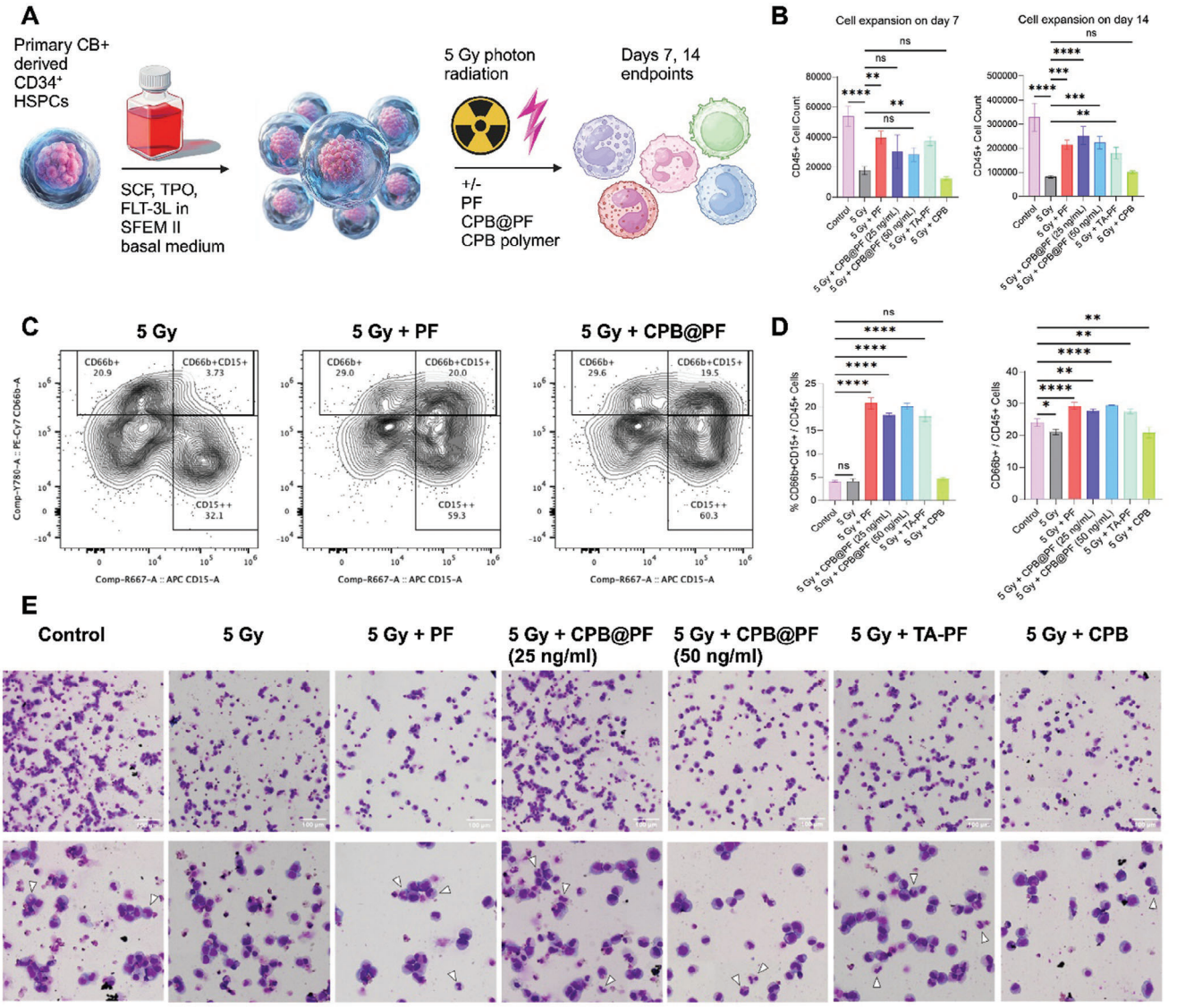


**Figure 4.** CPB@PF nanoparticles promote hematopoietic recovery in vitro using human HSPCs. (A) Schematic of experiments showing radiation exposure and protective drug administration on CB-HSPCs over two weeks. B) $CD45^+$ cell expansion in each respective group over two weeks. C) Flow cytometric gating strategy for $CD15^+CD66b^+$ granulocytes. Data represent the mean ± SD ($n = 3$, One-way ANOVA, $*p < 0.05$, $**p < 0.01$, $***p < 0.001$, $****p < 0.0001$). D) Quantification on day 7 of granulocytic and mature neutrophil populations. E) Wright-Giemsa staining of hematopoietic cells and differentiating neutrophils isolated from suspension cultures after 7 d post-radiation and post-drug administration. Scale bar, 100 µm. (arrows indicating the presence of multi-nucleated granulocytes in representative zoomed images).

intragastrically at a dose corresponding to approximately 150 µg of PF per mouse. As shown in the figure, the serum concentration of PF delivered via CPB@PF NPs reached a peak at the first measured time point and declined steadily over the next 72 h. In contrast, mice receiving 8.33 mg $kg^{-1}$ of free PF solution (i.g.) maintained a consistent serum PF concentration throughout the study, with levels hovering close to the detection limit.

To assess the biocompatibility and potential systemic toxicity of the NPs, the serum biochemical parameters were analyzed, revealing no significant nephrotoxicity or hepatotoxicity, as evidenced by unaltered levels of blood urea nitrogen (BUN) and alanine aminotransferase (ALT), respectively (Figure S26, Supporting Information). Moreover, the biochemical markers for kidney and liver function remained within the normal range across all study groups, including those treated with the CPB@PF.

We performed histological evaluations of the small intestine in mice exposed to irradiation doses of 0 and 7.25 Gy, collecting specimens on day 14 post-irradiation. Hematoxylin and eosin (H&E) staining showed morphological changes characteristic of radiation-induced damage. This included a marked loss of regenerative crypt cells and shortening of villi in the IR+PBS (i.g.), IR+CPB (i.g.), and IR+PF (i.g.) groups, indicative of substantial intestinal injury two weeks after irradiation (Figure 5D and Figure S28, Supporting Information). Orally administered PF failed to provide protective effects. In contrast, the CPB@PF-treated group displayed morphological improvements

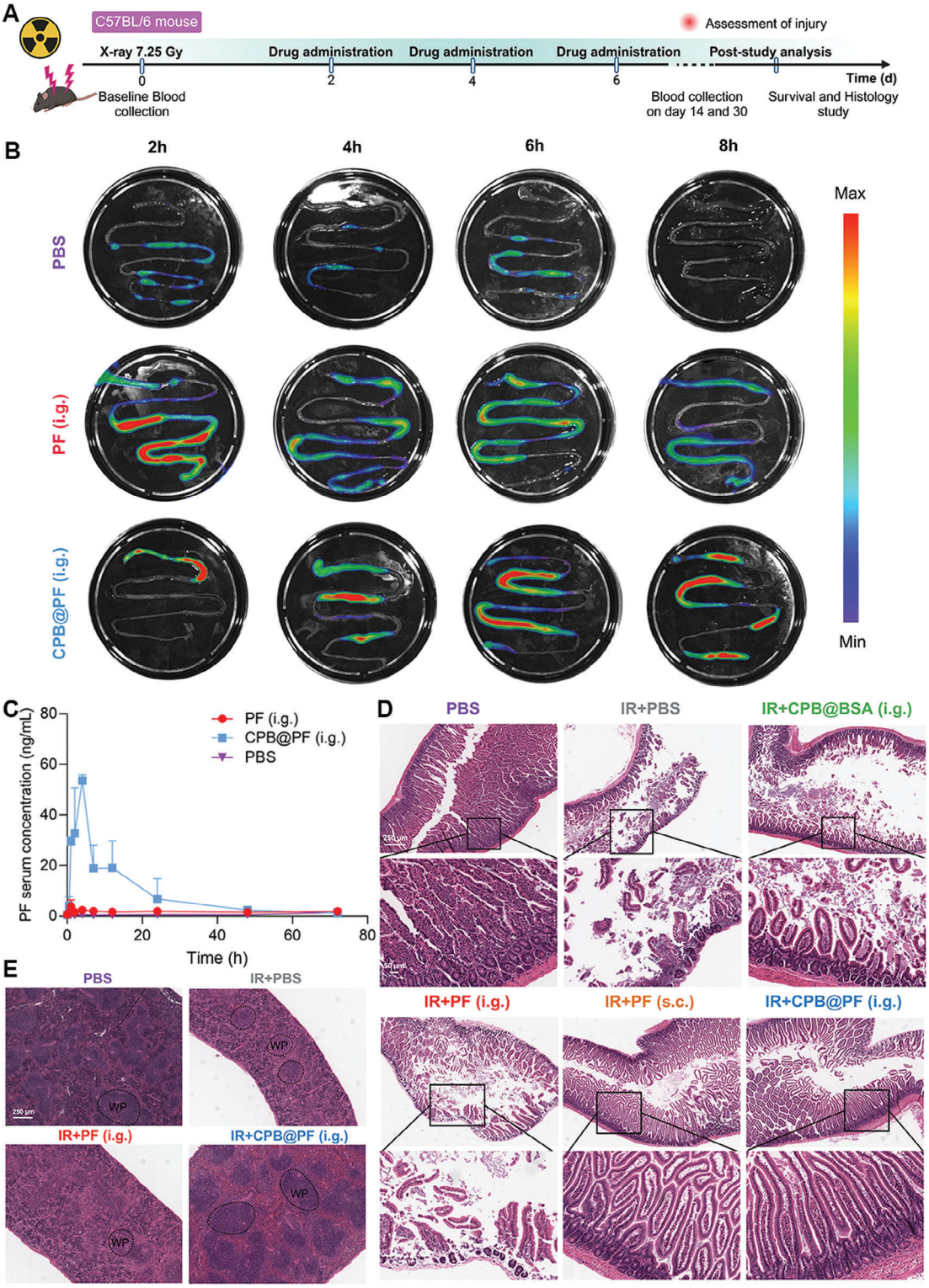


**Figure 5.** In vivo pharmacokinetics and efficacy of the CPB@PF system. CPB refers to $CP_{72\%}B_{24\%}$ selected for both in vivo and in vitro studies. A) Schematic illustration of the experiment protocol. B) Ex vivo fluorescence images of the intestines after oral administration of PBS, Cy5.5-PF, CPB@Cy5.5-PF NPs at different time points. C) Serum PF concentration for the CPB@PF system on C57BL/6 mice through oral gavage, compared with that of the PBS and native PF groups. D) Representative H&E-stained sections of intestinal tissues from the irradiated study groups. The top row provides an overall view (scale bar: 250 µm), while the bottom row offers a zoomed-in perspective (scale bar: 50 µm). E) Representative H&E-stained spleen tissue sections from irradiated study cohorts. The White Pulp, identified by dense, dark purple regions indicative of lymphoid tissue, is delineated by black dashed circles. Scale bar: 250 µm.

comparable to the unirradiated sham group, suggesting CPB@PF's potential in mitigating radiation-induced intestinal damage. In addition, in the H&E sections of spleen tissues for the same mice, the splenic architecture was near normal with white pulp containing well-developed, lymphocyte-rich follicles in the IR+CPB@PF (i.g.) group, as compared to the healthy and the IR+PF (s.c.) groups (Figure 5E and Figure S27, Supporting Information).

### 2.6. Therapeutic Effects on Radiation-Induced Hematopoietic Injury in Mice

Longitudinal monitoring of body weight in C57BL/6 mice revealed differential impacts of treatment groups. As shown in **Figure 6A**, the sham group (purple line), which was not exposed to radiation, exhibited consistent body weight throughout the 30 d observational period, serving as a control for typical weight stability. Mice exposed to fatal radiation without any drug treatment (gray line) demonstrated a severe decline in body weight, illustrating the impact of radiation without any treatment. The cohort receiving subcutaneous PF protein (gold-standard) showed resilience to radiation-induced weight loss. Mice treated with the CPB@BSA (polymer-only) displayed a similar trend to the no-drug group; notably, mice receiving CPB@PF NPs orally (blue line) demonstrated a stabilization of body weight similar to the subcutaneous PF and control group.

Survival analysis showed that mice treated with CPB@PF (i.g.) or PF (s.c.) had significantly higher survival rates compared to the control group (Figure 6B). Kaplan-Meier analysis revealed that the median survival time post-irradiation for the control group (IR+PBS) was approximately 15 d. In contrast, the CPB@PF (i.g.) group exhibited a notably higher survival rate than the control group (IR+PBS) throughout the 30 d observation period, with $p < 0.001$. These results correspond with the observed body weight trends. Importantly, the survival rate in the CPB@PF group was only slightly lower than that of the PF (s.c.) group, with 60% versus 80% survival at the experiment's conclusion. This outcome shows potential to increase both the dosage and frequency of CPB@PF administration, taking advantage of the convenience of oral delivery to potentially improve overall compliance.

The survival advantage observed in the CPB@PF (i.g.) and PF (s.c.) groups is further supported by the immune cell count data (Figure 6C–E). Mice treated with these formulations demonstrated elevated levels of white blood cells (WBCs), neutrophils, and lymphocytes compared to the control group. Specifically, the IR+PF (s.c.) group exhibited the highest immune cell counts across all categories, suggesting a robust protective effect against radiation exposure following subcutaneous administration of PF. The CPB@PF (i.g.) group also showed significantly elevated immune cell counts, though slightly lower than the subcutaneous group, indicating that oral administration is effective at stimulating an immune response, albeit potentially to a lesser degree.

In studying the development of hematopoietic malignancies and anemia post-irradiation, we were interested in understanding the induction and prevention of injury to the BM niche post-treatment. The images exhibited significant histopathological changes, particularly increased adipocyte proliferation, a known response to irradiation of hematopoietic tissues (Figure 6F). The groups treated with PBS and orally administered PF showed a pronounced increase in adipocyte content in the BM, indicating the adverse impact of radiation on the BM microenvironment and its regenerative capabilities. Conversely, the BM of groups treated with CPB@PF and PF (s.c.) showed substantially fewer adipocytes and a larger proportion of red (hematopoietic cell rich) marrow. To substantiate these findings quantitatively, we employed MarrowQuant, a machine learning-based method designed to augment BM evaluations in both research and clinical settings.[25] As depicted in Figure 6G and further quantified in Figure 6H,I, MarrowQuant semi-automatically determined the proportion of adipocyte and hematopoietic areas within the BM sections. The graphical representations corroborate our qualitative observations, showcasing that CPB@PF, particularly when administered orally, markedly diminishes radiation-induced adipogenesis within the BM. These findings could indicate the potential of our therapeutic approach in mitigating radiation-related BM injury, enhancing the regenerative potential of hematopoietic tissues following radiation exposure.

## 3. Discussion

Acute radiation syndrome poses a significant challenge in medical management following exposure to ionizing radiation, where the survival and recovery mainly depends on the restoration of the hematopoietic system.[26] The standard for ARS treatment has been largely confined to the administration of growth factors (GFs) and cytokines, a strategy that, while effective, encounters practical challenges in protracted, low dose exposures, as in space travel, as well as in mass casualty scenarios. The reliance on subcutaneous injections for the delivery of the four FDA-approved countermeasures may not be viable in situations where medical infrastructure is compromised. The advancement of oral delivery systems for these countermeasures could significantly broaden access to essential treatments following radiation exposure, a critical consideration in enhancing healthcare responses to deep space radiation exposures and nuclear incidents on Earth.

Our work introduces a new approach to this challenge, focusing on the development of an efficient oral formulation for the FDA-approved radioprotective agent G-CSF (in PEGylated form), demonstrating effectiveness even when first administered 48 h post-exposure. By leveraging a library of PBA-functionalized CP polymers, we have designed a versatile nanoparticle-based strategy for G-CSF delivery. This methodology uses tannic acid as an auxiliary mediator, enhancing protein stability and enabling the formation of uniform nanoparticles through the condensation of low-molecular-weight polymers.

Here, we describe using our nanoparticles and the base polymer (CPB) for mitigating ionizing radiation-induced ROS generation and injury to hematopoietic cells. Elevated oxidative stress is a significant concern in exposures to IR, generating high levels of mitochondria-dependent ROS that lead to cell cycle checkpoint arrest, apoptosis, and stress-related responses.[27] Chronic elevation in inflammatory cytokines post-exposure is also critical, with cytokines such as TNF-$\alpha$ and IL-6 playing a central role in sustained oxidative damage following IR exposure.[3,28] In this study, we noted varying levels of activation within TLR pathways in human cell types, including cardiomyocytes, cardiac fibroblasts, MSCs, and endothelial cells following

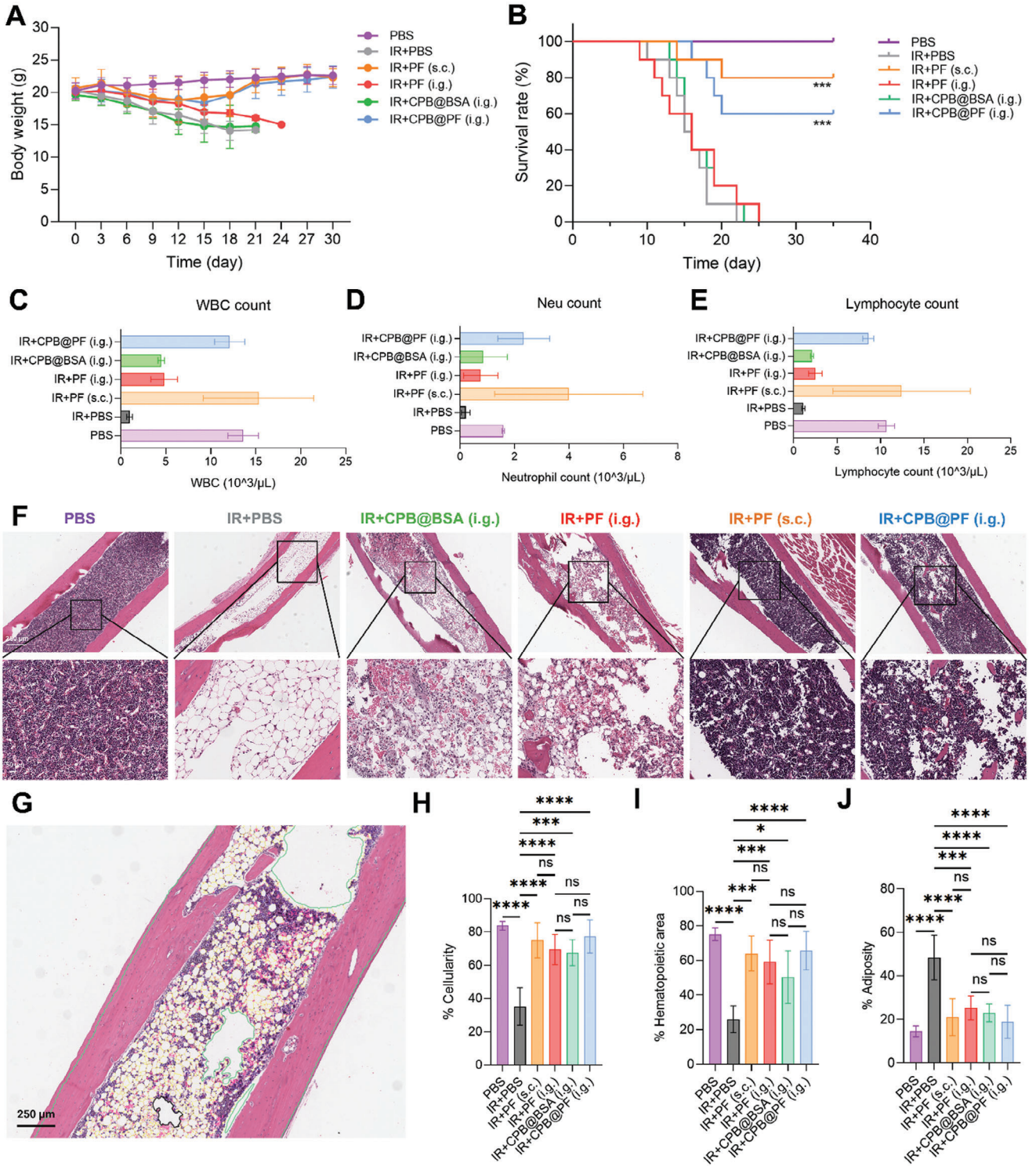


**Figure 6.** Response of C57BL/6 mice to a lethal dose of whole-body radiation (7.25 Gy; $n = 10$). CPB refers to $CP_{72\%}B_{24\%}$ selected for both in vivo and in vitro studies. A) Body weight changes across various treatment groups. B) Median survival rates for different groups: PBS (i.g.), undefined (>30 d); IR + PBS (i.g.), 15 d; IR + PF (s.c.), undefined (>30 d); IR + PF (i.g.), 16 d; IR + CPB (i.g.), 15 d. Survival differences were assessed using the Log-rank (Mantel-Cox) test. Significance levels are marked as follows: ***$p < 0.001$. C) White blood cell counts result of the indicated groups. D) Neutrophil counts result of the indicated groups. E) Lymphocyte counts result of the indicated groups. F) Representative H&E-stained sections of bone tissues from the irradiated study groups. Overall view (top, scale bar: 250 μm) and zoomed-in perspective (bottom, scale bar: 50 μm). G) Representative figure of bone section histology analyzed using MarrowQuant-based machine learning. MarrowQuant 2.0 outputs include: H) % cellularity, I) % hematopoietic area, and J) % adiposity of the analyzed bone marrow histology sections. Data are presented as mean ± SD (One-way ANOVA, **$p < 0.01$, ***$p < 0.001$, ****$p < 0.0001$).

irradiation. Previous studies, such as those by Takemura et al., have highlighted that inhibiting TLR3 can mitigate severe forms of radiation-induced gastrointestinal syndrome.[29] Moreover, overactivation of TLR4 has been identified as a risk factor in the advancement of radiation-induced liver disease, as evidenced by changes in the expression of key factors such as VEGFR-2, GM-CSF, and TRAIL within hepatic interstitial fluid.[30] TLR9 signaling has been implicated in TNF-$\alpha$-driven hemophagocytic syndrome in BM transplantation models, with TNF-$\alpha$ inhibition presenting a viable treatment approach.[31] The rationale for testing the CPB's effect on TLR inhibition stems from the recognition that TLR pathways are crucial mediators of the inflammatory response post-irradiation. By inhibiting these pathways, it is possible to reduce the chronic inflammatory and oxidative stress responses that exacerbate radiation-induced damage.

The integration of PBA moieties into our nanoparticles has been proven to significantly enhance the protection of protein payloads from physiological degradation, thus preserving their in vivo therapeutic efficacy. Additionally, the formation of the TA-protein complex is straightforward, requiring only the combination of protein and TA in an optimal stoichiometric molar ratio. Tannic acid itself is recognized for its biocompatibility, as well as its antibacterial and antioxidant attributes. Therefore, we consider tannic acid an important component of our nanosystem, as it achieves a comparably stable configuration in vivo with a minimal quantity of TA. The computational analysis and entropy measurement experiments further affirm the efficacy of this supramolecular approach. Other proteins, such as BSA and insulin, also form nanoparticles with favorable size distribution. Our findings demonstrate that the $CP_{72\%}B_{24\%}$@PF delivery system not only supports recovery from hematopoietic acute radiation syndrome but also reduces tissue damage in both in vivo and in vitro settings. Importantly, the low cytotoxicity profile of this nanosystem, as determined by screening assays on HSPCs, together with the lack of significant adverse effects in animal models treated with control nanoparticles, highlights its safety and therapeutic potential.

The implications of our research extend beyond H-ARS management. The CPB@protein nanosystem introduces a framework for the innovation of future therapeutics, serving as a platform for creating oral delivery systems applicable to a variety of biologic treatments. It also proposes the possibility of designing nanocarriers with therapeutic functions even in the absence of encapsulated cargoes. While there have been advancements in nanoparticle-based delivery systems, there is limited focus on the oral delivery of PEGylated proteins.[32] One of the most recent examples is the use of hydrogels for the delivery of PEGylated insulin.[32] Increased hydrophilicity of PEGylated proteins can reduce their affinity for chitosan, thereby complicating the formation of stable complexes.[33] Additionally, PEG attachment to solid surfaces nearly eliminates protein adsorption due to the strong hydration of PEG chains and the unfavorable entropy change associated with protein binding.[34] Studies have also shown that PEGylation decreases the adsorption affinity to silica.[34] To address these challenges, our work introduces a nanosystem assembled with tannic acid, designed to enhance stability and functionality.

Our CPB@protein system offers a solution by potentially enhancing the transport and absorption of PEGylated proteins, such as PF, through improved protection and opening of tight junctions. Moreover, the anti-inflammatory properties of our formulation could provide a synergistic therapeutic effect in treating H-ARS. By mitigating inflammatory responses and facilitating effective protein delivery, our nanosystem shows potential for improving outcomes in radiation-induced injuries and other inflammatory conditions.

Despite the potential of our nanoparticle system as a countermeasure for hematopoietic ARS, several areas require further improvement. Optimizing the large-scale production of nanoparticles with consistent quality and therapeutic properties is crucial for clinical translation. Future steps may involve the application of flash nanocomplexation (FNC) strategies to increase the yield and quality of CPB@PF nanoparticle synthesis.[35] Additionally, enhancing the therapeutic potential to ensure it surpasses the efficacy of subcutaneous injections is essential. Unlike radiation shielding nanoparticles (e.g., $WO_3$, BaO),[36] the long-term effectiveness of our system against protracted radiation exposure, such as in deep space missions, requires additional validation. Addressing these limitations is essential for advancing the practical application of this nanoparticle system in radiation countermeasures and broader medical contexts.

## 4. Conclusion

Our study presents a novel therapeutic approach for ARS, addressing both the logistical hurdles presented by existing treatment strategies and the complex biological consequences of radiation-induced damage. As we progress toward the clinical application of our findings, the CPB@PF system emerges as a promising solution for ARS treatment and management. In applications anticipated in deep space travel, CPB@PF NPs and other new therapeutic modalities can be investigated in space-relevant settings by using human, 3D in vitro organoid and organ-on-a-chip models both on Earth and in Space to mitigate the risks of simulated cosmic radiation.[5b,28c,37] We believe the technological advancements here will reduce the public health impact of nuclear and radiological emergencies, as well as providing a convenient radioprotective countermeasure for future deep space travel, underscoring the broader implications of our work for enhancing therapeutic delivery of future radioprotective drugs.

## 5. Experimental Section

*Study Design*: It is hypothesized that tannic acid-modified proteins could self-assemble with chitosan-based polymers to maintain cargo stability under acidic conditions and facilitate in vivo protein transport, enabling sustainable payload release into the bloodstream to alleviate acute radiation syndrome while ensuring patient compliance. To investigate this, molecular docking and molecular dynamic simulations were employed to study the nanoparticle assembly process. Tannic acids, ubiquitous plant secondary metabolites, possess various biological activities and are known to interact with proteins, altering their structure and properties. The focus was on determining the optimal amount of tannic acid to form TA–protein conjugates, which were then complexed with functionalized chitosan polymer for oral protein delivery. Animal studies were conducted with the approval of the Institutional Animal Care and Use Committee at Columbia University. To evaluate the nanosystem's biosafety, its cytotoxicity was examined using hematopoietic progenitor cells as a model and

performed biochemical profiles in C57BL/6 mice. Cell-free DNA binding and cellular studies were performed at least three times. For in vivo studies, 10 mice per group were used to assess the survival status under fatal irradiation conditions.

*QUANTI-Blue Assay of CPB Polymers*: HEK-Blue hTLR3, hTLR4, hTLR8, and hTLR9 reporter cells were used for the TLR activation and inhibition study. HEK-Blue hTLR cells grow as adherent cells. Detach the cells in the presence of pre-warmed phosphate buffered saline (PBS) by tapping the flask or using trypsin for 2–3 min at room temperature and then seeding to the 96 well plates for tests. For hTLR3 experiments, HEK-Blue hTLR3 reporter cells ($5\times10^4$ per well) in DMEM were seeded in a 96-well plate for 30 min, then 50 µL RT DAMP was added. At the same time, 10 µL CPB (4 µg per mL) was added. The cells treated with medium-only were used as a negative control; cells treated with poly(I:C) (1 µg per mL) were a positive control. After 24 h, cell supernatants were collected and incubated with QUANTI-Blue solution for 2 h. The embryonic alkaline phosphatase (SEAP) activity in each well was determined by measuring the OD at 620 nm with a plate reader. For the hTLR4 experiment, the cell number in each well was set at $2.5\times10^4$ per well. 1 µg $mL^{-1}$ of Lipopolysaccharide (LPS) was used as a positive control for hTLR4 activation. For hTLR8 and hTLR9 experiments, the cell number in each well was set at $4\times10^4$ and $8\times10^4$ per well, respectively. Imidazoquinoline R848 (1 µg $mL^{-1}$) and CpG BW006 (1 µg $mL^{-1}$) were used as positive controls for hLTR8 and hTLR9, respectively. The remaining methods were the same as described above for hTLR3.

*In Vitro Cytotoxicity Screening of CPB Polymers and CPB@PF NPs*: CB-derived hematopoietic stem and progenitor cells were seeded in 96-well plates at $5\times10^3$ cells per well with 100 µL StemSpan Serum-Free Expansion Medium (SFEM II) supplemented with 100 ng per mL SCF, TPO, and FLT3L (Peprotech) and incubated for 24 h prior to cytotoxicity tests. CPB polymers were dissolved in culture medium and were added to 96-well plates at a final concentration of 0.1–1000 µg $mL^{-1}$. All cells were incubated for another 24 h, then the culture medium was replaced with 100 µL of fresh medium containing 10 µL CCK-8 solution. After a 4 h incubation, the supernatant was collected to a new 96-well plate and the absorbance of each well at 450 nm was measured. Cells without treatment were used as a control. Each sample was tested in triplicate.

The live-dead assay was used to evaluate the in vitro cytotoxicity of CPB polymers and CPB@PF nanoparticles on cultured mammalian cells. The assay was conducted by treating semi-confluent layers of a human epithelial cell line with a range of concentrations of CPB polymers. Following a 24 h exposure period, the cells were stained with 100 µL of PBS buffer containing 2 µM Calcein and 4 µM ethidium homodimer-1 (EthD-1) to differentiate live cells under fluorescence microscopy. The cytotoxic effects of the polymers and nanoparticles were assessed by comparing the ratio of live to dead cells in treated samples against control groups.

*Molecular Docking*: The 3D structures of polymers for screening were drawn and optimized for conformation using ChemBio 3D. The crystal structure of pegfilgrastim was established by modeling crystal A0A4U1FI26 based on AlphaFold2 predictions, while the crystal structure of insulin was also derived from AlphaFold2 predictions. The structure of BSA was obtained from https://www.rcsb.org/structure/4F5S. These protein crystals were processed using the Protein Preparation Wizard module of Schrödinger software, which included protein preprocessing, regeneration of native ligand states, H-bond assignment optimization, protein energy minimization, and water removal. The prepared ligand compound was then docked into the active site of the pegfilgrastim protein using the highest precision XP docking. Lower docking scores indicated lower binding free energy and higher binding stability of the compound with the protein. The ligand compound underwent MM-GBSA calculation analysis with the pegfilgrastim protein's active site to estimate binding free energy, where lower binding free energy corresponded to higher binding stability. The flexible XP docking mode, which allows both the protein and ligand to adapt, was employed for these molecular docking calculations. Although this mode's complex algorithm requires longer computation times, it offers higher accuracy and reliability, making it particularly effective for identifying specific compounds or target molecules.

*Molecular Dynamic Simulations*: GROMACS 2020.6 was utilized for dynamic simulation. The system comprised one protein and tannic acid molecules. Simulations were conducted in a closed environment with a temperature of 289.15 K, a pH of 7, and a pressure of 1 bar. The pdb2gmx tool converted the receptor structure topology file into a GROMACS-compatible format using the AMBER99SB force field parameters. AmberTools facilitated the conversion of TA molecules into GROMACS-recognizable itp format topology files, employing the GAFF force field for ligand atom processing. TIP3P water molecules were added to simulate the aqueous environment, and NaCl was included to balance the system's charge. Following initial system construction, energy minimization was performed using the steepest descent method. Subsequently, with protein positions restrained, 100 ps NVT (constant number of particles, volume, and temperature) and 100 ps NPT (constant number of particles, pressure, and temperature) equilibrium simulations were conducted. Following NVT and NPT equilibrations, 200 ns production dynamics simulations were carried out for both the protein-23 TA and protein-TA systems with a timestep of 2 fs. Covalent bond lengths were constrained using the linear constraint solver algorithm, and long-range electrostatic interactions were addressed with the Particle Mesh Ewald (PME) method. Upon completion of all simulations, the gmx module was employed to calculate the radius of gyration (*Rg*) to assess system compactness, the root-mean-square deviation (RMSD) to monitor local conformational changes (with a fluctuation cutoff of 0.2), and the root mean square fluctuation (RMSF) to observe local conformational dynamics during the simulation.

*The Tight Junction ZO-1 Protein Staining*: Caco-2 cells were seeded on 96-well plates at a density of $2 \times 10^4$ cells per well in DMEM with 20% FBS and cultured in 5% $CO_2$ atmosphere at 37 °C. Then cells were washed twice with HBSS and incubated with different micelles. After 2 h of incubation at 37 °C, the cells were washed with PBS solution, further stained with 20 µL of Hoechst 33342 (1 mg $mL^{-1}$) and ZO-1 monoclonal antibody (ZO1-1A12), Alexa Fluor 488 for 10 min at 37 °C followed by washing three times with PBS, and fixed using 4% glutaraldehyde for 15 min. The tight junction ZO-1 protein was examined by a Nikon AXR MP confocal system. Continuity ratio was defined as the total number of skeletonized ZO-1 pixels divided by the number of disconnected skeleton segments, yielding a dimensionless index of tight-junction integrity.

*Mice and Total Body Irradiation (TBI)*: All in vivo animal studies were performed in compliance with the Institutional Animal Care and Use Committee (IACUC) of Columbia University and conducted under all relevant federal and state guidelines. Female C57BL/6 mice (8 weeks old) were purchased from the Jackson Laboratory and acclimated to the facility until they were approximately 14 weeks old. The mice were then randomly assigned to either the zero-dose sham group (0 Gy) or the irradiated group (7.25 Gy, total body exposure). Irradiation was performed using an X-Rad 320 machine (Precision X-Ray Inc., North Branford, CT). Prior to the experiment, dose and dose rates were calibrated using a National Institute of Standards and Technology (NIST)-traceable advanced Markus ion chamber and Unidos E electrometer (PTW, Freiburg, Germany). The X-Rad 320 machine was operated at 320 kV, with a current of 12.5 mA and a dose rate of 0.78 Gy $min^{-1}$ to deliver a total of 7.25 Gy. A custom Thoraeus filter (0.8 mm Sn, 0.3 mm Cu, 1 mm Al; HVL 3 mm Cu) was used during the irradiation. Calibration of the X-Rad 320 built-in transmission chamber was also performed using a Radcal ion chamber. Two days post-irradiation, the in vivo experiments commenced. Each individual mouse was considered the experimental unit in this study.

*In Vivo Oral PF Delivery Pharmacokinetics of CPB Polymer*: Female mice weighing 15–20 g were used for the pharmacokinetic studies. All animal procedures were approved by the Institutional Animal Care and Use Committee (IACUC) of Columbia University. Radiated mice were fasted overnight with free access to water before dosing. Mice were randomly divided into groups to receive either CPB@PF nanoparticles (i.g.), pure PF (i.g.), or saline solution as a negative control. Blood samples were collected from the tail vein at predetermined time points (0, 0.5, 1, 2, 4, 7, 12, 24, 48, and 72 h) post-administration. The serum was separated by centrifugation and stored at -80 °C until analysis. PF concentrations in serum were determined using human G-CSF standard ABTS ELISA development kit (Peprotech) following the manufacturer's instructions.

*Protective Effect against Intestinal and Bone Marrow Radiation Injury*: Female mice weighing 15–20 g were used for the pharmacokinetic studies. All animal procedures were approved by the Institutional Animal Care and Use Committee (IACUC) of Columbia University. Mice were randomly divided into groups ($n = 5$ per group) to receive either CPB@PF nanoparticles (i.g.), CPB@BSA nanoparticles (i.g.), pure PF (i.g.), pure PF (s.c.), or a saline solution as a negative control. The saline solution group without irradiation served as a sham group. The mice were exposed to 7.25 Gy of whole-body RT and treated with the drugs for a week. Afterward, on day 14, the small intestinal tissue and bone marrow tissue of mice were immediately collected and prepared for pathological examination. Also, the blood was collected in the EDTA tubes for measuring the complete blood count (CBC) test.

*Mouse Survival Study*: C57BL/6 mice were randomly divided into groups ($n = 10$ per group) to receive either CPB@PF nanoparticles (i.g.), CPB@BSA nanoparticles (i.g.), pure PF (i.g.), pure PF (s.c.) or a saline solution as a negative control. The saline solution group without irradiation was served as a sham group. The interventions were administered orally via gavage or by subcutaneous injection.

The health and behavior of the mice were monitored daily, and the survival time and body weight of each mouse were recorded. Mice were euthanized if they met the humane endpoint criteria established by the IACUC. The survival time for each mouse was used to construct Kaplan–Meier survival curves. The log-rank (Mantel-Cox) test was used to compare survival distributions between treated and control groups. Hazard ratios (HR) and 95% confidence intervals (CI) were calculated to assess the relative risk of mortality associated with the treatment. A $p$-value $< 0.05$ was considered statistically significant. All statistical analyses were performed using GraphPad Prism.

To assess the long-term safety, female C57BL/6 mice were treated with PBS, IR+PF (s.c.) and IR+CPB@PF (i.g.). After 30 d, the mice were euthanized, and their blood serum was collected for biochemical profile study.

*Histology*: For histological analysis, the intestines, spleens, and bone marrows were fixed overnight in 2% paraformaldehyde, transferred into gradient ethanol solutions, embedded into paraffin, and sectioned into slices with a thickness of 4 um. The obtained tissue sections were mounted onto glass slides and stained with hematoxylin and eosin, and then examined by an optical microscope by the Columbia Molecular Pathology Core.

*Machine-Learning Analysis of BM Slides Using MarrowQuant*: To assess the impact of radiation on bone marrow, we employed MarrowQuant, an adapted version of the original tool designed for human bone marrow assessment. The adapted MarrowQuant tool was implemented as a QuPath script. This integration allows for a seamless and automated analysis pipeline, enhancing the tool's accessibility and usability for researchers. Histology sections of bone marrow were collected from mice post-radiation treatment.[25a,38] The samples were fixed in formalin solution (histological tissue fixative, Sigma-Aldrich), decalcified, and embedded in paraffin for sectioning. Sections were 5 µm in thickness and stained for H&E by the Columbia Molecular Pathology Core. The MarrowQuant script was executed on the selected ROIs. The script automatically quantified various parameters, including cell density, trabecular bone volume, and adipocyte content.

The formulas for % cellularity, % hematopoietic area, and % adiposity are as follows:

$$\%\ \text{Cellularity} = \frac{\text{Hematopoietic area (Hm.Ar)}}{\text{Hematopoietic area (Hm.Ar)} + \text{Total adipocytic area (Tt.Ad.Ar)}} \times 100 \quad (1)$$

$$\%\ \text{Hematopoietic area} = \frac{\text{Hematopoietic area (Hm.Ar)}}{\text{Marrow area (Ma.Ar)}} \times 100 \quad (2)$$

$$\%\ \text{Adiposity} = \frac{\text{Total adipocytic area (Tt.Ad.Ar)}}{\text{Marrow area (Ma.Ar)}} \times 100 \quad (3)$$

*Statistical Analysis*: All experiments were carried out in triplicates unless otherwise noted specifically, and all results are represented as means ± SD. Statistical analyses were performed using Student's unpaired t test for comparisons between two groups, and multiple comparisons were conducted using one-way analysis of variance (ANOVA) with the Bonferroni test. All statistical analyses were calculated using GraphPad Prism and OriginPro software, and statistical significance was set at $*p < 0.05$, $**p < 0.01$, $***p < 0.001$, $****p < 0.0001$.

## Supporting Information

Supporting Information is available from the Wiley Online Library or from the author.

## Acknowledgements

The authors gratefully acknowledge the funding support of this work by the Translational Research Institute for Space Health (TRISH/NASA) agency (RAD0104 and NNX16A069A to G.V.N., D.J.B., and K.W.L.), National Institute of Allergy and Infectious Diseases (5 U19 AI067773 to D.J.B.), National Institutes of Health (NRSA 1F31CA275733 to D.N.T.), and National Science Foundation (GRFP 1644869 to D.N.T.). The authors thank the staff at Columbia's Center for Radiological Research for their assistance in running ionizing radiation equipment. These studies used the resources of the Herbert Irving Comprehensive Cancer Center Confocal and Specialized Microscopy Shared Resource funded in part through Center Grant P30CA013696, as well as support from the HICCC Molecular Pathology Core with support from Kevin Sun and Dr. Hanina Hibshoosh. Flow cytometry was performed with support of the Columbia Stem Cell Initiative Flow Cytometry core facility at Columbia University Irving Medical Center, under the direction of Michael Kissner, and was supported by the Office of the Director, National Institutes of Health under Award Number S10OD026845. The authors also thank the support of Chai Hoon Quek, Sue Halligan, and Connie Chen, for technical support related to laboratory tools. A subset of figures was created in BioRender.com.

## Conflict of Interest

The authors declare no conflict of interest.

## Author Contributions

Y.Z. and D.N.T. contributed equally to this work. K.W.L. and G.V.-N. conceived the study and provided overall supervision of the study. Y.Z. and D.N.T. designed the experiments. Y.Z., D.N.T., H.W., S.H., and X.Q. analyzed and interpreted data. Y.Z. and D.N.T. wrote the manuscript. Y.Z., D.N.T., H.W., S.H., Z.Z., N.Y., D.T., D.N., I.B., X.W., S.A.A., G.G., D.J.B., G.V.-N., and K.W.L. edited the manuscript. Y.Z., B.P., X.W., H.W., and Z.Z. performed irradiation experiments. S.A.A., G.G., D.J.B., G.V.N., and K.W.L. provided additional supervision. All authors reviewed, contributed to and approved the paper.

## Data Availability Statement

The data that support the findings of this study are available from the corresponding author upon reasonable request.

## Keywords

hematopoietic acute radiation syndrome, inflammation, oral protein delivery, pegfilgrastim, phenylboronic acid, radiation countermeasures, tannic acid

Received: November 6, 2024
Revised: January 13, 2025
Published online:

[1] E. H. Donnelly, J. B. Nemhauser, J. M. Smith, Z. N. Kazzi, E. B. Farfan, A. S. Chang, S. F. Naeem, *South. Med. J.* **2010**, *103*, 541;
[2] V. K. Singh, V. L. Newman, T. M. Seed, *Cytokine* **2015**, *71*, 22;
[3] V. K. Singh, T. M. Seed, *Int. J. Radiat. Biol.* **2021**, *97*, 1526;
[4] L. Sihver, S. Mortazavi, in 2019 IEEE Aerospace Conf., IEEE, Piscataway, NJ **2019**, p. 1, https://ieeexplore.ieee.org/abstract/document/8742175?casa_token=OzwVyMXbQNMAAAAA:m-OK2vj1IWKcYKG20NSUfNs-inZfNFoMhAfL6YNLZMgvoXXevVd1ED1f9qjq2QfkAg86qgM.
[5] a) D. N. Kernagis, E. Balcer-Kubiczek, S. Bazyar, C. M. Orschell, I. L. Jackson, *Life Sci. Space Res.* **2022**, *35*, 36; b) R. S. Bokhari, A. Beheshti, S. E. Blutt, D. E. Bowles, D. Brenner, R. Britton, L. Bronk, X. Cao, A. Chatterjee, D. E. Clay, *Life Sci. Space Res.* **2022**, *35*, 105;
[6] R. Arora, R. Chawla, R. Marwah, V. Kumar, R. Goel, P. Arora, S. Jaiswal, R. K. Sharma, *J. Pharm. Bioallied Sci.* **2010**, *2*, 202;
[7] P. Rofail, M. Tadros, R. Ywakim, M. Tadrous, A. Krug, L. E. Cosler, *Expert Rev. Pharmacoecon. Outcomes Res.* **2012**, *12*, 699;
[8] K. G. Hankey, A. M. Farese, E. C. Blaauw, A. M. Gibbs, C. P. Smith, B. P. Katz, Y. Tong, K. L. Prado, T. J. MacVittie, *Radiat. Res.* **2015**, *183*, 643;
[9] G. Molineux, *Curr. Pharm. Des.* **2004**, *10*, 1235;
[10] C. H. Ridyard, D. M. Dawoud, L. V. Tuersley, D. A. Hughes, *Patient-Patient-Cent. Outcomes Res.* **2016**, *9*, 281;
[11] Y. Yun, Y. W. Cho, K. Park, *Adv. Drug Delivery Rev.* **2013**, *65*, 822;
[12] T. D. Brown, K. A. Whitehead, S. Mitragotri, *Nat. Rev. Mater.* **2020**, *5*, 127;
[13] S.-Y. Yin, Y. Hu, J. Zheng, J. Li, R. Yang, *ACS Appl. Mater. Interfaces* **2022**, *14*, 50583;
[14] a) A. Baldwin, B. W. Booth, *J. Biomater. Appl.* **2022**, *36*, 1503; b) Z. He, T. Nie, Y. Hu, Y. Zhou, J. Zhu, Z. Liu, L. Liu, K. W. Leong, Y. Chen, H.-Q. Mao, *J. Controlled Release* **2020**, *318*, 86;
[15] D. R. Jacobson, O. A. Saleh, *Nucleic Acids Res.* **2017**, *45*, 1596;
[16] T. Bus, A. Traeger, U. S. Schubert, *J. Mater. Chem. B* **2018**, *6*, 6904;
[17] R. Zhang, X. Qin, F. Kong, P. Chen, G. Pan, *Drug Delivery* **2019**, *26*, 328;
[18] a) N. Yoshinaga, T. Ishii, M. Naito, T. Endo, S. Uchida, H. Cabral, K. Osada, K. Kataoka, *J. Am. Chem. Soc.* **2017**, *139*, 18567; b) A. Stubelius, S. Lee, A. Almutairi, *Acc. Chem. Res.* **2019**, *52*, 3108; c) Q. Wang, Y. Yang, D. Liu, Y. Ji, X. Gao, J. Yin, W. Yao, *Nano Lett.* **2021**, *21*, 6022;
[19] T. Miyamoto, K. Tsuchiya, K. Numata, *Nanoscale* **2021**, *13*, 5679;
[20] A. Kumari, S. K. Yadav, *Expert Opin. Drug Delivery* **2011**, *8*, 141;
[21] S. Gilbert, R. Zhang, L. Denson, R. Moriggl, K. Steinbrecher, N. Shroyer, J. Lin, X. Han, *EMBO Mol. Med.* **2012**, *4*, 109;
[22] a) B. Srinivasan, A. R. Kolli, M. B. Esch, H. E. Abaci, M. L. Shuler, J. J. Hickman, *J. Lab. Autom.* **2015**, *20*, 107; b) K. Benson, S. Cramer, H.-J. Galla, *Fluids Barriers CNS* **2013**, *10*, 5;
[23] T.-H. Yeh, L.-W. Hsu, M. T. Tseng, P.-L. Lee, K. Sonjae, Y.-C. Ho, H.-W. Sung, *Biomaterials* **2011**, *32*, 6164.
[24] P. Okunieff, S. G. Swarts, B. Fenton, S. B. Zhang, Z. Zhang, L. Rice, D. Zhou, F. Carrier, L. Zhang, *Radiat. Res.* **2024**, *202*, 70;
[25] a) R. Sarkis, O. Burri, C. Royer-Chardon, F. Schyrr, S. Blum, M. Costanza, S. Cherix, N. Piazzon, C. Barcena, B. Bisig, *Mod. Pathol.* **2023**, *36*, 100088; b) J. Vercellino, B. Małachowska, S. Kulkarni, B. I. Bell, S. Shajahan, K. Shinoda, G. Eichenbaum, A. K. Verma, S. P. Ghosh, W.-L. Yang, *Stem Cell Res. Ther.* **2024**, *15*, 123;
[26] H. Guo, W.-C. Chou, Y. Lai, K. Liang, J. W. Tam, W. J. Brickey, L. Chen, N. D. Montgomery, X. Li, L. M. Bohannon, *Science* **2020**, *370*, eaay9097;
[27] M. Xiao, M. H. Whitnall, *Curr. Mol. Pharmacol.* **2009**, *2*, 122;
[28] a) R. Yahyapour, P. Amini, S. Rezapour, M. Cheki, A. Rezaeyan, B. Farhood, D. Shabeeb, A. E. Musa, H. Fallah, M. Najafi, *Mil. Med. Res.* **2018**, *5*, 9; b) D. N. Tavakol, T. R. Nash, Y. Kim, S. He, S. Fleischer, P. L. Graney, J. A. Brown, M. Liberman, M. Tamargo, A. Harken, *Biomaterials* **2023**, *301*, 122267; c) D. N. Tavakol, T. R. Nash, Y. Kim, P. L. Graney, M. Liberman, S. Fleischer, R. I. Lock, A. O'Donnell, L. Andrews, D. Ning, *Adv. Sci.* **2024**, *11*, 2401415;
[29] N. Takemura, T. Kawasaki, J. Kunisawa, S. Sato, A. Lamichhane, K. Kobiyama, T. Aoshi, J. Ito, K. Mizuguchi, T. Karuppuchamy, *Nat. Commun.* **2014**, *5*, 3492;
[30] a) W. Zhi-Feng, Z. Le-Yuan, Z. Xiao-Hui, G. Ya-Bo, Z. Jian-Ying, H. Yong, Z. Zhao-Chong, *Radiat. Res.* **2014**, *182*, 674; b) B. H. Rhieu, M. W. Epperly, S. Cao, J. Goff, D. Shields, D. Franicola, H. Wang, J. S. Greenberger, *In Vivo* **2014**, *28*, 441; c) C. Engelmann, A. Habtesion, M. Hassan, A. J. Kerbert, L. Hammerich, S. Novelli, M. Fidaleo, A. Philips, N. Davies, S. Ferreira-Gonzalez, *J. Hepatol.* **2022**, *77*, 1325;
[31] J. Liu, Y.-M. Guo, N. Onai, H. Ohyagi, M. Hirokawa, N. Takahashi, H. Tagawa, K. Ubukawa, I. Kobayashi, H. Tezuka, *Biol. Blood Marrow Transp.* **2016**, *22*, 627;
[32] A. D. Tuesca, C. Reiff, J. I. Joseph, A. M. Lowman, *Pharm. Res.* **2009**, *26*, 727;
[33] a) R. Gref, A. Domb, P. Quellec, T. Blunk, R. Müller, J.-M. Verbavatz, R. Langer, *Adv. Drug Delivery Rev.* **2012**, *64*, 316; b) J. Wei, D. B. Ravn, L. Gram, P. Kingshott, *Colloids Surf., B* **2003**, *32*, 275;
[34] S. S. Pai, T. M. Przybycien, R. D. Tilton, *Langmuir* **2010**, *26*, 18231;
[35] K. Li, Y. Wang, Y. Xu, G. Shi, S. Wei, X. Zhang, B. Zhang, Q. Jia, H. Xu, L. Yu, *Chin. Chem. Lett.* **2024**, *35*, 109511;
[36] M. T. Alresheedi, M. Elsafi, Y. T. Aladadi, A. F. Abas, A. B. Ganam, M. Sayyed, M. A. Mahdi, *Polymers* **2023**, *15*, 2160;
[37] M. Arzt, M. Mozneb, S. Escopete, J. Moses, A. Sharma, *Stem Cells Dev.* **2024**, *33*, 143;
[38] J. Tratwal, D. Bekri, C. Boussema, R. Sarkis, N. Kunz, T. Koliqi, S. Rojas-Sutterlin, F. Schyrr, D. N. Tavakol, V. Campos, *Front. Endocrinol.* **2020**, *11*, 480.